

---

# Noninvasive NMR and NIRS Measurement of Vascular and Intracellular Oxygenation In Vivo

# 8

Youngran Chung and Thomas Jue

---

## 8.1 Introduction

In the canonical biochemical view, respiration requires a coordinate regulation of oxygen transport, carbon unit flux, electron flow, proton pumping, and ADP translocation. Certainly in-vitro experiments have supported the paradigm, cast in terms of either a kinetic or thermodynamic model [1]. Yet, in blood-perfused tissue the specific regulatory mechanisms still remain unclear [2, 3]. In contrast to isolated mitochondria or cells, many overlapping reactions intervene to regulate cellular bioenergetics [4].

In particular, muscle alters dramatically its bioenergetics during sudden transition from rest to work. As such, muscle can serve as a convenient model to study how the cell regulates dynamically its metabolism and oxygen consumption ( $\text{VO}_2$ ): upon initiation of contraction, the immediate rise in cellular energy demand triggers a rapid adaptation in the ventilatory, cardiovascular, and peripheral blood flow response to enhance  $\text{O}_2$  flux. How the cell mobilizes its metabolic resources, increases its metabolic rates, and adjusts  $\text{O}_2$ /nutrient flux pose central questions in the theory of respiratory control. Although some researchers downplay a significant role for a metabolic regulation of  $\text{VO}_2$  and point to a tight match between  $\text{O}_2$  supply throughout contraction, others have contended that metabolism must modulate  $\text{VO}_2$  demand and blood flow [5].

From the vantage of cellular bioenergetics, experiments have measured metabolic fluxes and have analyzed the results to discriminate kinetic versus thermodynamic control [1]. Specifically, in the kinetic model, a substrate such as ADP limits the reaction rate [2]. Since muscle contraction consumes ATP, the model predicts that the product of ATP hydrolysis, ADP, regulates the rate of respiration to match the rate of energy utilization. In contrast, the thermodynamic model posits a balanced change in key metabolite levels, which act conjointly to regulate respiration.

However, in-vivo NMR myocardium studies have failed to confirm these simple ideas. Elevating  $\text{VO}_2$  does not elicit any rise in ADP, as derived from the  $^{31}\text{P}$  signals of PCr and ATP [6–8]. This observation does not align precisely with the prediction of either the kinetic or thermodynamic models. In contrast, skeletal muscle shows a drop in PCr level during contraction and an ADP-dependent  $\text{VO}_2$  [9]. But the ADP-dependent rise in  $\text{VO}_2$  does not appear at the initial phase of muscle contraction [10].

---

Y. Chung, M.D., Ph.D. (✉) • T. Jue, Ph.D. (✉)  
Biochemistry and Molecular Medicine, University of California Davis, 95616-8635 Davis, CA, USA  
e-mail: [yrcchung@ucdavis.edu](mailto:yrcchung@ucdavis.edu); [tjue@ucdavis.edu](mailto:tjue@ucdavis.edu)

Resolving these discordant observations requires an accurate assessment of intracellular  $\text{VO}_2$  and the  $\text{O}_2$  supply. Because whole body  $\text{VO}_2$  and arterial venous oxygen difference measurements with a mean end capillary blood flow have limited accuracy in determining the dynamic change in  $\text{VO}_2$  in localized myocytes, researchers have explored noninvasive in-vivo techniques, such as near-infrared spectroscopy (NIRS) and nuclear magnetic resonance (NMR) [11, 12]. Certainly, air-breathing animals require  $\text{O}_2$  to survive. But how the cell modulates its  $\text{O}_2$  utilization to meet a physiological range of energy demand remains an open question.

---

## 8.2 Microelectrode Measurement of Vascular and Intracellular Oxygenation

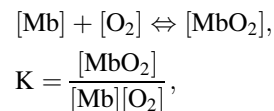
A simple, direct approach to measuring tissue  $\text{O}_2$  utilizes microelectrodes. These electrodes are usually comprised of a platinum wire with a recessed cathode tip of  $\sim 1 \mu\text{m}$ . They respond to changes in  $\text{O}_2$  within 25 ms. For in-vivo application, however, they have potential limitations. They can inflict tissue damage, have low spatial and temporal resolution, might consume oxygen at the cathode to alter the tissue environment, and can introduce artifacts arising from fluid convection or by variation in oxygen transport [13–17]. Moreover, any rigorous interpretation of the in-vivo experimental data requires sophisticated mathematical models to guide the analysis [18, 19]. These concerns limit the use of  $\text{O}_2$  electrodes to study human subjects during dynamic movement. Nevertheless,  $\text{O}_2$  microelectrode studies in animal models have revealed unique physiological insights: tissue has a lower  $\text{pO}_2$  than venous blood, which implies the presence of heterogeneous distribution of oxygen in the microcirculation [20].

---

## 8.3 Spectroscopic Approaches

Instead of using microelectrodes to measure  $\text{O}_2$  in tissue, other techniques have used the signals from oxygen-binding heme proteins: myoglobin (Mb) and hemoglobin (Hb). Hb exists exclusively in the vasculature, while Mb localizes in the cytoplasm of myocytes. Upon binding  $\text{O}_2$ , the electronic configuration of the heme  $\text{Fe}^{2+}$  converts from a paramagnetic to a diamagnetic state. Because the electronic configuration and protein structure of the oxygenated and deoxygenated heme protein differ, the associated spectroscopic signatures can characterize the different oxygenation states. Given the relative ratio of deoxy-Mb or deoxy-Hb (dMb or dHb) and oxy-Mb or Hb ( $\text{MbO}_2$  or  $\text{HbO}_2$ ) signals, a calculation using the in-vitro association ( $K_a$ ) or dissociation constants ( $K_d$ ) of  $\text{O}_2$  binding to myoglobin and hemoglobin leads to a value for the partial pressure of oxygen ( $\text{pO}_2$ ) in the vascular and/or cellular space.

Association of  $\text{O}_2$  from Mb follows the expressions



where  $[\text{MbO}_2]$  is the concentration of oxy-Mb,  $[\text{Mb}]$  is the concentration of deoxy-Mb,  $[\text{O}_2]$  is free  $\text{O}_2$ , and  $K$  is the dissociation constant. Since Mb binds a single  $\text{O}_2$ , the  $\text{O}_2$  saturation of Mb becomes

$$S_{\text{MbO}_2} = \frac{[\text{MbO}_2]}{[\text{Mb}] + [\text{MbO}_2]} = \frac{K[\text{Mb}][\text{O}_2]}{[\text{Mb}] + K[\text{Mb}][\text{O}_2]},$$

where  $S_{\text{MbO}_2}$  is the fraction of Mb saturated with  $\text{O}_2$ . Converting the equation in terms of  $p\text{O}_2$  and  $P_{50}$  (the partial pressure of oxygen and partial pressure of oxygen that saturates half the Mb, respectively) transforms the equation into

$$S_{\text{MbO}_2} = \frac{K[\text{O}_2]}{1 + K[\text{O}_2]} = \frac{[\text{O}_2]}{\frac{1}{K} + [\text{O}_2]} = \frac{p\text{O}_2}{P_{50} + p\text{O}_2},$$

For Hb, the equation includes exponent  $n$  (the Hill coefficient) to account for the additional heme  $\text{O}_2$ -binding sites in tetrameric Hb:

$$S_{\text{HbO}_2} = \frac{K[\text{O}_2]^n}{1 + K[\text{O}_2]^n} = \frac{[\text{O}_2]^n}{\frac{1}{K} + [\text{O}_2]^n} = \frac{p\text{O}_2^n}{P_{50} + p\text{O}_2^n}.$$

Many studies have determined the  $\text{O}_2$  binding curve of Mb and HbA (normal human adult Hb), characterized by its  $\text{O}_2$  affinity (specified usually in terms of its  $P_{50}$ ) and Hill coefficient. Monomeric Mb has a  $P_{50}$  of 2.3 mmHg at  $35^\circ\text{C}$ , with  $n = 1$ . HbA has a  $P_{50}$  of about 26 mmHg and can take Hill coefficient values from 1 to 4. For HbA, experiments have determined a Hill coefficient around 2.8 and have interpreted it as an index of protein cooperativity [21].

For in-vivo application, blood volume alteration can confound the analysis. Because muscle contraction elicits vasodilatation and vasoconstriction, blood volume can change and modulate overall spectrum intensity without shifting the ratio of the oxy- and deoxyhemoglobin signals. Monitoring overall spectral intensity changes in the oxy- and deoxy-Hb signal provides an index of relative blood volume change. Alternatively, following the isosbestic points in the transition from oxy- to deoxy-Hb can also help delineate blood volume from oxygenation changes (vide infra). The ratio of deoxy-Hb/HbO<sub>2</sub> reflects the oxygenation state.

## 8.4 Hb Absorbance of Visible Light

Figure 8.1 displays the typical spectra from both deoxy-Hb (dHb) and HbO<sub>2</sub> in part of the visible spectral region 450–650 nm. For HbA, the HbO<sub>2</sub> spectrum shows a distinct Soret band ( $\gamma$ ) at 415 nm (not shown). Two additional peaks ( $\alpha$  and  $\beta$  bands) appear at 577 and 541 nm. As oxygen levels decrease, the Soret  $\gamma$  band shifts from 415 toward 430 nm, while the  $\alpha$  and  $\beta$  bands gradually disappear.

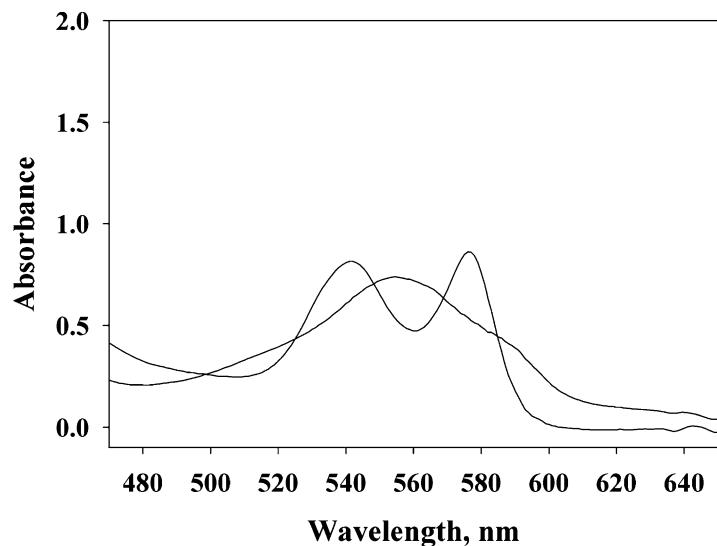


**Fig. 8.1** Visible spectra of HbO<sub>2</sub> and deoxy-Hb. HbO<sub>2</sub> has peak maxima at 541 and 577 nm, and deoxy-Hb has a signal maximum at 555 nm

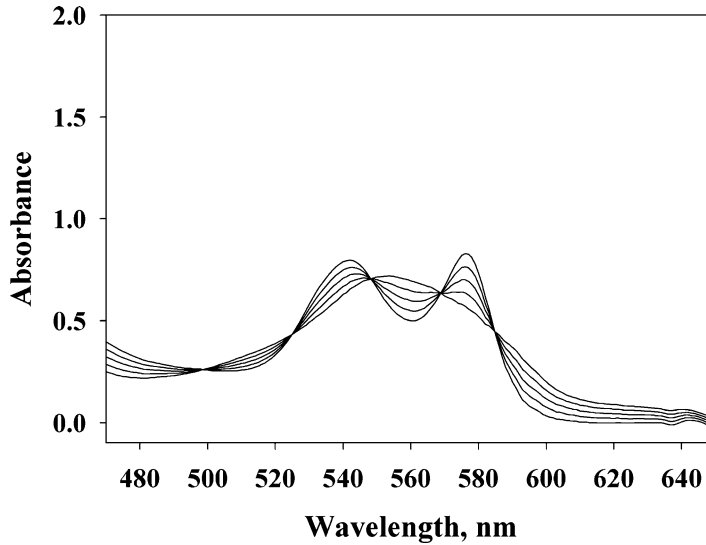


**Fig. 8.2** Spectra simulating the Hb signals at varying HbO<sub>2</sub>/deoxy-Hb molar ratios: 1:9, 3:7, 5:5, 7:3, 9:1. The spectra reflect the varying levels of blood oxygenation. Isosbestic points occur at 498, 525, 548, 568, and 585 nm. Signal intensity at the HbO<sub>2</sub> and deoxy-Hb maxima vary, but the isosbestic points remain invariant

A new peak from dHb emerges at 555 nm. The HbO<sub>2</sub> ( $\alpha$  and  $\beta$  bands), the deoxy-Hb signal, the HbO<sub>2</sub> signal, and the association or dissociation constant ( $K_a$  or  $K_d$ ) lead to a determination of  $pO_2$ .

Figure 8.2 models a bank of HbO<sub>2</sub> and dHb spectra during transition from the deoxygenated to the oxygenated state. The signal at 555 nm decreases as the signals at 541 and 577 nm increase, as the HbO<sub>2</sub>/deoxy-Hb molar ratios increase: 1:9, 3:7, 5:5, 7:3, 9:1. Even though the HbO<sub>2</sub> and deoxy-Hb signal intensities change with oxygenation, the spectra intersection points or isosbestic points at 498, 525, 548, 568, and 585 nm remain invariant. However, if the overall Hb signal concentration or volume increase, as observed during vasodilation, the isosbestic points will rise. Figure 8.3 shows a factor of twofold increase in blood at HbO<sub>2</sub>/deoxy-Hb molar ratios 1:9, 3:7, 5:5, 7:3, and 9:1, respectively. Compared with Fig. 8.1, the overall spectral intensity has increased by a factor of two, as reflected in the isosbestic points, but the signal intensity ratio of HbO<sub>2</sub> and deoxy-Hb remains the same. The isosbestic points then provide a way to normalize Hb saturation with respect to the total Hb pool.

## 8.5 Mb Absorbance of Visible Light

Because both Mb and Hb have Fe-protoporphyrin IX as the prosthetic group and share protein structural features, such as a proximal and a distal histidine near the Fe center, the porphyrin  $\pi - \pi^*$  transition ( $a_{1u}, a_{2u}$  to  $e_g$  ( $\pi^*$ )) gives rise to a similar Soret band as well as the  $\alpha$  and  $\beta$  bands (sometimes referred to as the  $Q_o$  and  $Q_v$  bands) [22]. For MbO<sub>2</sub>, the  $\alpha$  and  $\beta$  bands appear at 580 and 542 nm. For HbO<sub>2</sub>, the corresponding bands also appear around 580 and 542 nm and exhibit similar extinction coefficients. Separating the MbO<sub>2</sub> and HbO<sub>2</sub> signals in the visible spectra of blood-perfused muscle then poses a formidable challenge. In contrast, brain tissue has no Mb to interfere with Hb detection. Nevertheless, the Hb and Mb signals reflect the distinct vascular versus intracellular oxygenation.

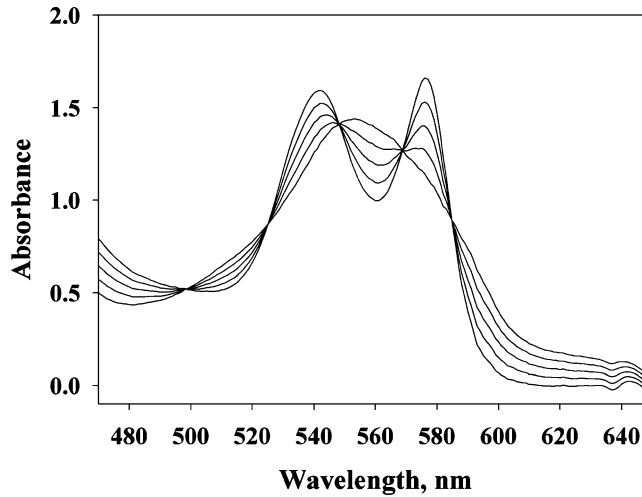


**Fig. 8.3 Spectra simulating blood volume and Hb oxygenation changes.** The overall HbO<sub>2</sub> and deoxy-Hb signals will increase with blood volume. The visible spectra reflect a twofold increase in total blood volume at different HbO<sub>2</sub>/deoxy-Hb molar ratios: 1:9, 3:7, 5:5, 7:3, 9:1, respectively. In comparison to Fig. 8.2, the isosbestic points occur at the same wavelengths, but the intensity has risen by a factor of 2. The ratios of HbO<sub>2</sub>/deoxy-Hb signal intensities, however, remain the same

For in-vitro assay, many studies have employed a Reynafarje algorithm to discriminate Mb from Hb, which is predicated on the specific spectral features of MbCO and HbCO [23]. Because HbCO displays a  $\beta$ -to- $\alpha$  intensity ratio of 1, while MbCO shows a ratio of about 0.8, the signal intensity difference at 568 and 538 nm for a mixture of MbCO and HbCO can factor out the Mb concentration in samples extracted from blood-perfused tissue:

$$A_{538} - A_{568} = (\epsilon_{538\text{HbCO}} - \epsilon_{568\text{HbCO}})C_{\text{HbCO}} + (\epsilon_{538\text{MbCO}} - \epsilon_{568\text{MbCO}})C_{\text{MbCO}}.$$

Since  $\epsilon_{538\text{HbCO}} = \epsilon_{568\text{HbCO}}$ ,

$$C_{\text{MbCO}} = \frac{A_{538} - A_{568}}{\epsilon_{538\text{MbCO}} - \epsilon_{568\text{MbCO}}} = \frac{A_{538} - A_{568}}{14.7 \times 10^3 - 11.8 \times 10^3} = (A_{538} - A_{568}) \times 3.45 \times 10^{-4} \text{ M}.$$

Despite its simple elegance, an unmindful application of the Reynafarje algorithm without an appropriate calibration and baseline adjustment can lead to an erroneous determination of the Mb concentration and a consequent misinterpretation of Mb function [24]. Moreover, the  $\epsilon_{538\text{HbCO}} = \epsilon_{568\text{HbCO}}$  condition doesn't always hold; the values for  $\epsilon_{538\text{MbCO}} - \epsilon_{568\text{MbCO}}$  vary with different species, and small changes in the spectral baseline will distort the analysis.

## 8.6 Near-Infrared Versus Visible Light Scattering

Using visible light to follow vascular or intracellular changes in pO<sub>2</sub>, however, appears limited by its shallow (millimeter) penetration depth. Light propagation attenuates ( $\mu_t$ ) by scattering ( $\mu_s$ ) and absorbance ( $\mu_a$ ) interactions with molecules in the medium, as expressed by

$$\mu_t = \mu_s + \mu_a,$$

where  $1/\mu_t$  defines the mean free path, the mean distance a molecule travels, before it encounters any scattering or absorbance interaction.

Water dominates in most biological tissue and represents about 70–80% of overall content (~55 M). It represents the major source for scattering

Water also has a broad absorbance with a peak around 1,000 nm. As a result, the water signal contributes significantly to the NIRS spectra from 750 to 1,400 nm. The scattering coefficient ( $\mu_s$ ) also has a specific dependence upon wavelength:

$$\mu_s = A\lambda^{-P},$$

where  $A$  is the scattering amplitude and  $P$  is the scattering power.  $A$  reflects the scattering strength.  $P$  relates to scattering particle average size. For particles with diameter  $d$ , much smaller than the wavelength of light ( $d \ll \lambda$ ), the Rayleigh scattering limit  $P = 4$ .  $P$  decreases with increasing particle size (Mie scattering). The ratio  $R$  of light penetration depths at wavelengths  $\lambda_1$  and  $\lambda_2$  ( $\lambda_1 < \lambda_2$ ), at a specific  $P$ , and with the scattering coefficients, follows the equation

$$R = \frac{\mu_t^{\lambda_2}}{\mu_t^{\lambda_1}} = \frac{\mu_s^{\lambda_1} + C\mu_a^{\lambda_1}}{\left(\frac{\lambda_1}{\lambda_2}\right)^P \mu_s^{\lambda_1} + C\mu_a^{\lambda_2}}.$$

This equation indicates that scattering will decrease as wavelength increases. Penetration depth will increase correspondingly. Specifically, using NIRS instead of visible light extends the penetration depth from a millimeter to the centimeter range [25–27].

Indeed, with a typical source–detector separation of 3 cm, NIRS will detect signals from a banana-shaped volume centered approximately 1.5 cm below the surface [28]. A larger spacing between source and detector will sample signals from a deeper volume. For brain studies, spatial- and time-resolved NIRS experiments have ascribed 55% and 69% of the detected signal arising from cerebral tissue. Several reviews have discussed NIRS signal quantification, advantages/limitations, and biomedical applications [29–31].

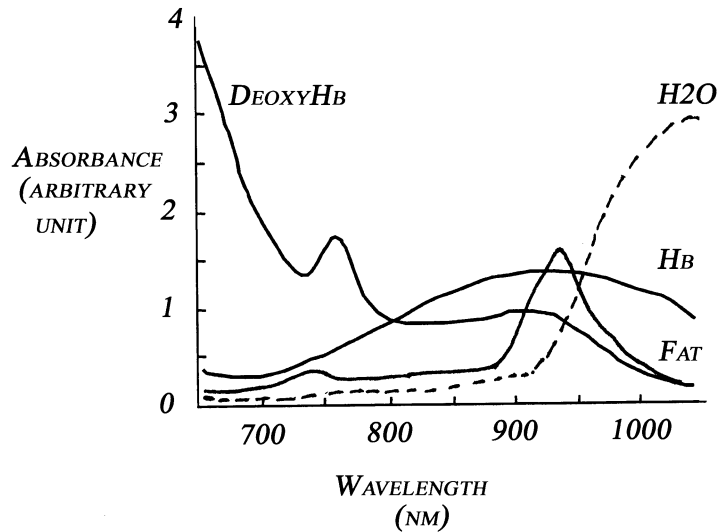
---

## 8.7 Interference from Fat Layer

Hb also absorbs near-infrared light (750–1,400 nm) (Fig. 8.4). DHb has a well-defined absorbance maximum at 760 nm. In contrast, HbO<sub>2</sub> has a broad absorbance extending from 750 to 1,000 nm. Many NIRS instruments use the absorbance at 850 nm to denote the HbO<sub>2</sub> concentration, partly because it skirts the lipid signal centered at 940 nm and the intense water signal at 1,000 nm (Fig. 8.4).

Lipid, however, has a near-infrared absorbance. It interferes prominently in tissue with high ratios of lipid to Hb and with thick fat layers. Because subcutaneous tissue contains a high concentration of fat, the extent of interference also depends on penetration depth. With close optode spacing, the detected NIRS signal has a significant contribution from the shallow layers containing subcutaneous fat. As optode spacing increases to sample signals from deeper tissue, fat interference decreases. This variation in fat contribution based on optode spacing provides a basis for deconvoluting HbO<sub>2</sub> from the fat signal. Such an approach produces a linear intensity relationship with penetration depth using signals from optode separation at 7, 20, 30, and 40 mm. The 7-mm spaced optodes also help to minimize the skin effect. Monte Carlo simulations confirm the strategy to deconvolute the fat layer signal. With the fat correction algorithm, the coefficient of variation (standard deviation/mean) for the NIRS HbO<sub>2</sub> signal in exercising muscle decreases from 40–50% to 11–21% [32, 33].

**Fig. 8.4** Representative 650–1,050 nm traces denoting the contribution from HbO<sub>2</sub>, deoxy-Hb, fat, and water



## 8.8 Overlapping Mb and Hb Signals

As in the case of the visible spectrum, the Mb and Hb NIRS signals overlap. Some researchers have ascribed no significant role for Mb to supply O<sub>2</sub> during muscle contraction. Because Mb has an extremely high affinity for O<sub>2</sub>, it cannot readily release its O<sub>2</sub> store. Hb must then supply all the O<sub>2</sub> from the very onset of contraction [34–36]. Others have assumed that NIRS monitors predominantly Hb oxygen saturation and desaturation kinetics. As a consequence, the NIRS observed change ( $\Delta[\text{deoxy}]$ ) arises from the capillary blood flow adjustment, which supports a school of thought that envisions a change in the gradient from capillary O<sub>2</sub> to the muscle that precisely matches O<sub>2</sub> demand (VO<sub>2</sub>) [37, 38]. Indeed, many NIRS experiments assume a dominant Hb contribution [29, 39]. NMR and modeling experiments, however, show that Mb does desaturate and can contribute significantly to the NIRS signal.

Even though the signals overlap, Mb and Hb do exhibit slight spectral differences. Under ideal conditions, a second-derivative transformation reveals the spectral differences and provides the basis for a wavelength shift analysis to distinguish Mb from Hb [40]. Such an approach shows that Hb contributes 20% to the NIRS signal from human muscle, but 87% from mouse muscle.

NIRS measurements during contraction, however, introduce prominent motional artifacts, which would compromise the accuracy and precision of the wavelength shift analysis approach. Many researchers simply filter or smooth out these noise artifacts during data analysis. Others have culled these cyclic NIRS signals to determine vascular oxygenation during muscle contraction [41].

Most commercial NIRS instruments utilize the diffusion equation and the absorption coefficients ( $\mu_a$ ) to derive muscle oxygen saturation (SmO<sub>2</sub>). The solution to this equation assumes a particular geometry, such as a homogenous semiinfinite half-space geometry, and an optode configuration, and requires experimental input parameters to determine the absorption coefficients ( $\mu_a$ ). The  $\mu_a$  measured at multiple wavelengths then leads to tissue oxygen saturation via the Beer-Lambert law. However, the model assumption of a homogenous medium quickly departs from experiment reality since the fat and skin layers introduce inhomogeneities in muscle. Muscle, skin, and fat layers will attenuate light.

## 8.9 NMR

$^1\text{H}$  NMR can also monitor cellular and vascular oxygenation by following the signals of cytosolic myoglobin and blood hemoglobin [42]. A comparative analysis of NIRS and NMR data would clarify the relative contributions in the NIRS spectra.

Myoglobin is composed of approximately 153 amino acids and has a molecular weight of 17,500. It has an 85% helical structure and contains eight distinct segments (A–H). The iron in the prosthetic heme group coordinates oxygen with a binding affinity about ten times higher than that of Hb [21]. Despite the conservation of key residues, the primary sequence shows extensive variability across species [43]. How the primary, secondary, and tertiary structures modulate myoglobin's binding affinity for oxygen poses the central question in protein structure–function studies [44]. Mammalian hemoglobin also has a heme prosthetic group in each of its four subunits.

Under physiological conditions, the heme Fe exists predominantly in the +2 oxidation state. Ligated with oxygen, the heme Fe(II) electrons become paired ( $S = 0$ ) or diamagnetic. Unligated with oxygen, the heme Fe(II) electrons become unpaired ( $S = 2$ ) or paramagnetic [45]. The unpaired electrons in the paramagnetic state interact with the proton and produce a hyperfine shift in the NMR signal. Such a hyperfine interaction can originate from either a contact (through bond) or pseudocontact (through space) contribution [46, 47].

$$\left(\frac{\Delta H}{H}\right)_{\text{hyperfine}} = \left(\frac{\Delta H}{H}\right)_{\text{contact}} + \left(\frac{\Delta H}{H}\right)_{\text{pseudocontact}},$$

where  $H$  is the magnetic field,  $(\Delta H/H)_{\text{hyperfine}}$  is the overall hyperfine interaction,  $(\Delta H/H)_{\text{contact}}$  is the contact contribution, and  $(\Delta H/H)_{\text{pseudocontact}}$  is the dipolar or pseudocontact contribution.

In the contact mechanism, the hyperfine shift depends upon an electron–nuclear coupling and the molecular orbital overlap:

$$\left(\frac{\Delta H}{H}\right)_{\text{con}} = -A \frac{g\beta S(S+1)}{3\gamma kT},$$

where  $A$  is the electron–nuclear coupling constant,  $\beta$  is the Bohr magneton,  $\gamma$  is the magnetogyric ratio,  $g$  is the Lande constant,  $S$  is the spin quantum number,  $k$  is Boltzmann's constant, and  $T$  is the absolute temperature.

In the pseudocontact mechanism, the unpaired electron generates a dipole field:

$$\left(\frac{\Delta H}{H}\right)_{\text{pcon}} = \frac{1}{3R^3} \left\{ (1 - 3\cos^2\theta)(X_{zz} - \frac{1}{2}(X_{xx} + X_{yy})) + \sin^2\theta \cos 2\Omega(X_{yy} - X_{xx}) \right\},$$

where  $R$  is the internuclear distance,  $\theta$  and  $\Omega$  are angles in the molecular axis system, and  $X_{nn}$  ( $n = x, y, z$ ) are diagonal elements of the magnetic susceptibility tensor.

The contact shift reflects the through bond, the molecular orbital interaction, while the pseudocontact shift reflects the through space, the dipole interaction. Separating the contributions can pose some technical challenges [48, 49]. The paramagnetism also gives rise to a bulk magnetic susceptibility, given by the Curie law:

$$X = \frac{Ng^2\beta^2 S(S+1)}{3kT} = \frac{C}{T},$$



where  $N$  is the number of spins,  $g$  is Lande's constant,  $\beta$  is the Bohr magneton,  $S$  is the spin quantum number,  $k$  is Boltzmann's constant, and  $T$  is the absolute temperature.

## 8.10 Assignment of the Proximal Histidyl $N_{\delta}H$ Signal

Model compound and mutant protein studies have led to specific NMR assignments. In particular, the model study of 2-methyl imidazole axially coordinated to tetraphenylporphyrin (TPP) led to assignment of the proximal histidyl  $N_{\delta}H$  signal of Mb and Hb [50]. The exchangeable 2-methyl imidazole attached to the paramagnetic  $Fe^{2+}$  has its  $N_{\delta}H$  signal appearing at  $\sim 80$  ppm. In deuterated solvent, the signal disappears. Its hyperfine shift originates predominantly from electron delocalization via the contact shift mechanism. Magnetic anisotropy, associated with the dipolar shift mechanism, contributes only about 10%.

Indeed,  $^1H$  NMR studies of deoxygenated Mb and Hb have detected exchangeable signals at  $\sim 80$  ppm and have assigned them to the proximal histidyl  $N_{\delta}H$  [51, 52]. Mb shows one signal. Because of the inequivalence of the  $\alpha$  and  $\beta$  subunits, HbA exhibits two proximal histidyl  $N_{\delta}H$  signals. At  $25^{\circ}C$ , HbA exhibits signals at 76 and 64 ppm, corresponding to the  $\beta$  and  $\alpha$  subunits, respectively [53]. The corresponding signal for human myoglobin appears at 81 ppm [54]. Upon oxygenation, the signal disappears (see Fig. 8.5).

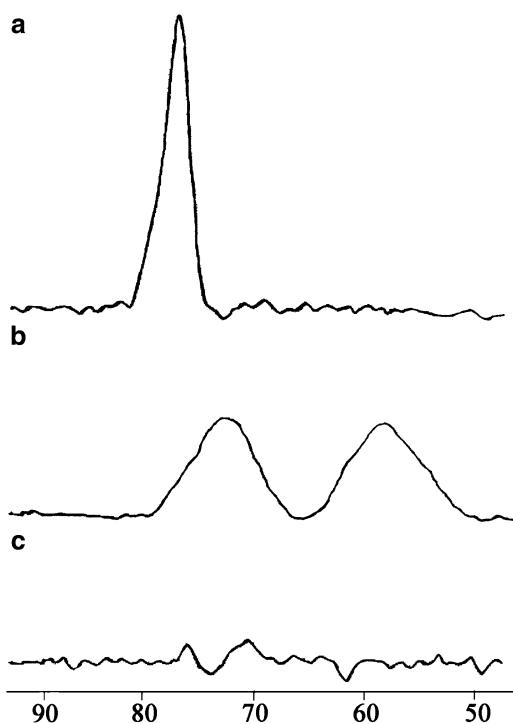


**Fig. 8.5**  $^1H$  NMR spectra in the region of 80 ppm. (a) Human muscle tissue under resting condition. No detectable deoxy-Mb signal; (b) proximal histidyl  $N_{\delta}H$  signals from  $\alpha$  (64 ppm) and  $\beta$  (76 ppm) subunits of deoxy-Hb in erythrocyte; (c) deoxy-Mb proximal histidyl  $N_{\delta}H$  signal (80 ppm) from human gastrocnemius muscle after cuffing the blood flow

Although the proximal histidyl N<sub>δ</sub>H proton can exchange with water, the exchange lifetime spans over a long NMR timescale. For deoxy-HbA the proximal histidyl NH exchange half-life occurs on the order of minutes to hours [55]. The α heme pocket has greater solvent accessibility than the β subunit.

---

### 8.11 Assignment of the Val E11 CH<sub>3</sub> Signal

The π delocalized electrons in the diamagnetic MbO<sub>2</sub> create a local magnetic field that interacts with local amino-acid residues in the heme pocket and shifts their resonance position. In particular, the Mb Val E11 γ1 CH<sub>3</sub> near the distal side of the heme experiences a significant ring current shift to -2.8 ppm [56]. The corresponding Hb α and β Val E11 γ1 CH<sub>3</sub> residues experience a similar shift to -2.39 ppm [57]. Because CO and O<sub>2</sub> bind to the heme Fe in different geometric configurations and will alter the local magnetic field, the Val E11 signals of MbCO and HbCO have altered resonance positions: MbCO (-2.40 ppm), HbCO-α (-1.70 ppm), and HbCO-β (-1.82 ppm) [53]. These upfield Val E11 signals decrease with decreasing oxygenation.

---

### 8.12 NMR and Measurement of Tissue Oxygenation

<sup>1</sup>H NMR can detect Mb Val E11 and proximal histidyl N<sub>δ</sub>H signals in cardiac and skeletal muscle in vivo. During hypoxia or ischemia, Mb releases O<sub>2</sub> in the myocytes, as reflected in the rising signal of deoxy-Mb proximal histidyl N<sub>δ</sub>H or the decreasing signal of Val E11 [58–61]. The decreasing intracellular O<sub>2</sub> level implicates a widening O<sub>2</sub> gradient from the capillary to the cell to facilitate O<sub>2</sub> flux into the cell [59, 61, 62]. Whether the gradient continues to widen or plateaus with increasing energy demand remains moot. Nevertheless, Mb desaturates with a rapid kinetics, consistent with a transient mismatch of O<sub>2</sub> supply and demand [10].

Contrary to the viewpoint of some researchers, Mb can contribute significantly to the NIRS signal. Indeed, perfused hindquarter muscle shows a dynamic range of Mb and Hb deoxygenation during graded levels of exercise intensity under blood and buffer perfusion. The results indicate that the NIRS signal contains a major contribution from Mb. Mb rapidly desaturates at the onset of muscle contraction and the intracellular oxygen level decreases proportionately with increasing work, with no observable plateau [62].

Because NMR can detect the distinct Mb and Hb signals of Val E11 and the proximal histidyl N<sub>δ</sub>H, it can help shed light on the contribution of Mb versus Hb in the NIRS signal and the role of O<sub>2</sub> supply and utilization in respiratory regulation during contraction. In fact, the respiration difference during exercise in normal versus heart failure subjects does not arise from a deficient O<sub>2</sub> supply. Instead, it appears to originate from an inadequate O<sub>2</sub> utilization in mitochondria [63].

When blood flow to the human gastrocnemius muscle decreases, the NMR spectra clearly exhibit the deoxy-Mb signal at 78 ppm, which rises as oxygenation decreases. Upfield at 73 ppm a signal corresponding to the deoxy-Hb β-subunit histidyl F8 N<sub>δ</sub>H appears and reaches a steady-state level [59]. Under the same experimental protocol, the kinetics of Mb desaturation matches the NIRS-observed decline in the composite MbO<sub>2</sub> and HbO<sub>2</sub> signal. Even after Mb has attained a steady-state level, the high-energy phosphate levels, as reflected in the <sup>31</sup>P spectra, remain unperturbed.

Because Hb and Mb desaturation kinetics depends critically on the cuffing and exercise protocols, comparative NIRS and NMR analysis has validity only when the data originate from a consistent set of experiments with well-defined cuffing protocols. Using the observation of a fast NIRS desaturation kinetics from one experiment and a slow NMR Mb desaturation kinetics from another to argue against

a significant Mb contribution in the NIRS signal would not constitute a compelling argument [64]. Another combined  $^1\text{H-NMR}$  and NIRS study using human and canine muscles also ascribes more than 50% of the NIRS signal to Mb [65]. A computer model indicates that the Mb contribution can represent 53–86% of the overall NIRS signal [66].

---

### 8.13 Mechanism of Respiratory Control

The kinetics of Mb and Hb desaturation during exercise at different workloads would yield invaluable insights into the canonical view of respiratory control, which posits a tight coordination of electron flow, proton pumping,  $\text{O}_2$  supply/delivery, metabolic flux, and an ADP-dependent feedback control.

In-vitro experiments certainly support the standard paradigm, cast in either a kinetic or a thermodynamic model. In blood-perfused tissue, however, numerous reaction steps can intervene to regulate respiration [2]. The sudden energy demand during muscle contraction stimulates both cellular metabolism and an  $\text{O}_2$  delivery. How the cell adapts to this surge in energy demand stands central to the question of respiratory control. Unfortunately, NIRS at present does not yield definitive insight, since it cannot easily distinguish intracellular from vascular  $\text{O}_2$  or  $\text{VO}_2$ .

$^1\text{H-NMR}$  studies have already shown an approach to map the intracellular  $\text{pO}_2$  with the Mb signals in vivo [58, 67, 68]. These NMR studies have reported fully saturated  $\text{MbO}_2$  in resting muscle, implying that the resting myocyte  $\text{pO}_2$  is well above an Mb  $\text{P}_{50}$  of 2.93 mmHg, a  $\text{pO}_2$  necessary to obtain 50%  $\text{O}_2$  saturation of Mb. Under these conditions,  $\text{O}_2$  most likely saturates cytochrome oxidase [69]. Raising the cellular  $\text{pO}_2$  cannot directly enhance the cytochrome oxidase kinetics, which mirrors the  $\text{VO}_2$ . In fact, human gastrocnemius muscle studies show a decrease, not an increase, in  $\text{pO}_2$  during exercise, in agreement with the cryosection analysis of canine gracilis muscle [59, 70]. In contrast, seal muscle during apnea shows Mb desaturation as blood flow and respiration decrease [61]. The intracellular  $\text{O}_2$  supply then decreases when respiration either increases or decreases. As such, the  $\text{O}_2$  supply alone cannot govern respiration rate in a simple fashion.

Although the fall in cellular  $\text{pO}_2$  increases the  $\text{O}_2$  gradient from capillary to cell,  $\text{O}_2$  delivery from the cytosol to mitochondria must increase to accommodate increasing  $\text{O}_2$  demand. A switch from free  $\text{O}_2$  diffusion to Mb-facilitated diffusion to deliver  $\text{O}_2$  to mitochondria could potentially compensate the falling  $\text{pO}_2$  during muscle contraction. However, tissues with inhibited Mb function or without Mb do not exhibit any apparent handicap in respiration [71–73].

Indeed, during muscle contraction  $\text{MbO}_2$  desaturates rapidly to a steady state with a time constant of 30 s. The desaturated steady-state levels rise with workload, but the kinetics time constant remains unchanged. Such rapid Mb desaturation implies that respiration does not operate necessarily in a kinetically slow way, consistent with an Eadie-Hofstee kinetic analysis of the intracellular  $\text{VO}_2$  (based on Mb desaturation kinetics) versus ADP, which reveals no ADP-dependent regulation at the onset of muscle contraction [10].

---

### 8.14 Summary

$^1\text{H-NMR}$  can follow the distinct Mb and Hb signals and provide a basis for deconvoluting these signals in NIRS spectra [74]. Because the near-infrared method has a higher signal sensitivity than magnetic resonance, it can detect changes in vascular and intracellular  $\text{O}_2$  more sensitively and on a faster timescale. However, NIRS has a much shallower penetration depth than NMR. A combined NMR and NIRS approach would help resolve many questions about the coordination of vascular and

metabolic controls to meet the rapidly changing energy demand during muscle contraction, which in turn would provide invaluable insight into pressing questions about respiratory control under in-vivo conditions [74].

**Acknowledgments** We would like to acknowledge funding support from NIH GM 58688, and the Japan Society for the Promotion of Science, Bilateral Programs (7301001471) for help in writing the chapter and in obtaining some of the data described herein.

---

## Problems

- 8.1. Marine mammals have a much higher concentration of Mb in their skeletal muscle than terrestrial mammals. What is the typical Mb concentration range in marine and terrestrial mammals? Why would an increase in Mb concentration confer a more prominent role for Mb facilitated O<sub>2</sub> diffusion? Discuss the role of Mb-facilitated O<sub>2</sub> diffusion in terms of O<sub>2</sub> diffusivity, Mb diffusivity, O<sub>2</sub> concentration, and Mb concentration in marine and terrestrial mammal myocytes. Assume identical O<sub>2</sub> and Mb diffusivity in all muscle cells.
- 8.2. A <sup>1</sup>H NMR experimental measurement of the deoxy-Mb signals in human gastrocnemius muscle shows no deoxy-Mb at rest. When the subject starts plantar flexion exercise at the rate of 70 contractions per minute, the deoxy-Mb signal appears and rises exponentially, consistent with the monoexponential relationship,  $y = c - c^* \exp(-x/\tau)$  ( $y$  = Mb concentration (mM),  $x$  = time (sec),  $\tau$  = time constant (sec), and  $c$  = arbitrary constant (mM)). During the first 2 min of exercise, venous pO<sub>2</sub> does not change, suggesting that almost all of the initial increase in muscle O<sub>2</sub> consumption arises from O<sub>2</sub> released from intracellular Mb. If  $\tau = 30$  s, what is the mitochondrial respiration rate at the onset of plantar flexion exercise? What does the mitochondrial respiration at the onset of muscle contraction imply about the contribution of oxidative phosphorylation? Use a gastrocnemius Mb concentration estimate of 0.4 mM.

---

## Further Reading

- Ferrari M, Muthalib M, Quaresima V (2011) The use of near-infrared spectroscopy in understanding skeletal muscle physiology: recent developments. *Philos Trans R Soc A* 369:1–14
- Gros G, Wittenberg BA, Jue T (2010) Myoglobin's old and new clothes: from molecular structure to function in living cells. *J Exp Biol* 213:2713–2725

---

## References

1. From AH, Zimmer SD, Michurski SP, Mohanakrishnan P, Ulstad VK, Thoma WJ, Uğurbil K (1990) Regulation of the oxidative phosphorylation rate in the intact cell. *Biochemistry* 29(15):3731–3743
2. Chance B, Leigh JS, Kent J, McCully K, Niokam S, Clark BJ, Maris JM, Graham T (1986) Multiple controls of oxidative metabolism in living tissues as studied by phosphorus magnetic resonance. *Proc Natl Acad Sci U S A* 83:9458–9462
3. Erecinska M, Wilson DF (1982) Regulation of cellular metabolism. *J Membr Biol* 70:1–14
4. Heineman FW, Balaban RS (1990) Control of mitochondrial respiration in the heart in vivo. *Annu Rev Physiol* 52:523–542
5. Tschakovsky ME, Hughson RL (1999) Interaction of factors determining oxygen uptake at the onset of exercise. *J Appl Physiol* 86(4):1101–1113
6. Balaban RS, Kantor HL, Katz LA, Briggs RW (1986) Relation between work and phosphate metabolites in the in vivo paced mammalian heart. *Science* 232:1121–1123

7. Heineman FW, Kupriyanov VV, Marshall R, Fralix TA, Balaban RS (1992) Myocardial oxygenation in the isolated working rabbit heart as a function of work. *Am J Physiol* 262:H255–H267
8. Kreutzer U, Merkhamer Y, Tran TK, Jue T (1998) Role of oxygen in limiting respiration in the in situ myocardium. *J Mol Cell Cardiol* 30(12):2651–2655
9. Barstow TJ, Buchthal SD, Zanonato S, Cooper DM (1994) Changes in potential controllers of human skeletal muscle respiration during incremental calf exercise. *J Appl Physiol* 77:2169–2176
10. Chung Y, Mole PA, Sailasuta N, Tran TK, Hurd R, Jue T (2005) Control of respiration and bioenergetics during muscle contraction. *Am J Physiol Cell Physiol* 288(3):C730–C738
11. Wagner PD (1995) Muscle O<sub>2</sub>. *Med Sci Sports Exerc* 27(1):47–53
12. Whipp BJ, Wasserman K (1972) Oxygen uptake kinetics for various intensities of constant-load work. *J Appl Physiol* 33(3):351–356
13. Albanese RA (1971) Use of membrane-covered oxygen cathodes in tissue. *J Theor Biol* 33:91–103
14. Whalen WJ, Nair P, Gainfield RA (1973) Measurements of oxygen tension in tissues with a micro oxygen electrode. *Microvasc Res* 5:254–262
15. Albanese RA (1973) On microelectrode distortion of tissue oxygen tensions. *J Theor Biol* 38:143–154
16. Whalen WJ, Riley J, Nair P (1967) A microelectrode for measuring intracellular pO<sub>2</sub>. *J Appl Physiol* 23:798–801
17. Whalen WJ (1980) A hypodermic needle PO<sub>2</sub> electrode. *J Appl Physiol* 48:186–187
18. Lubbers DW (1969) The meaning of the tissue oxygen distribution curve and its measurement by means of Pt electrodes. *Prog Respir Res* 3:112–123
19. Inch WR (1958) Problems associated with the use of the exposed platinum electrode for measuring oxygen tension in vivo. *Can J Biochem Physiol* 36(10):1009–1021
20. Duling BR, Berne RM (1970) Longitudinal gradients in periarteriolar oxygen tension: a possible mechanism for the participation of oxygen in local regulation of blood flow. *Circ Res* 27:669–678
21. Antonini E, Brunori M (1971) Hemoglobin and myoglobin in their reactions with ligands. Elsevier/North Holland, Amsterdam
22. Owens JW, Connor CJ (1988) Characterization of some low spin complexes of ferric hemeoctapeptide from cytochrome C. *Inorg Chim Acta* 151:107–116
23. Reynafarje B (1963) Simplified method for the determination of myoglobin. *J Lab Clin Med* 61:138–145
24. Masuda K, Truscott K, Lin PC, Kreutzer U, Chung Y, Sriram R, Jue T (2008) Determination of myoglobin concentration in blood-perfused tissue. *Eur J Appl Physiol* 104(1):41–48
25. van Staveren HJ, Moes CJM, Prahl SA, van Gemert MJC (1991) Light scattering in Intralipid-10% in the wavelength range of 400–1100 nm. *Appl Opt* 30:4507–4514
26. Mourant JR, Fuselier T, Boyer T, Johnson TM, Bigio J (1997) Predictions and measurements of scattering and absorption over broad wavelength ranges in tissue phantoms. *Appl Opt* 36:949–957
27. Pogue BW, Patterson MS (2006) Review of tissue simulating phantoms for optical spectroscopy, imaging and dosimetry. *J Biomed Opt* 11:041102–041116
28. Strangman G, Boas DA, Sutton JP (2002) Non-invasive neuroimaging using near-infrared light. *Biol Psychiatry* 52:679–693
29. McCully K, Hamaoka T (2000) Near-infrared spectroscopy: what can it tell us about oxygen saturation in skeletal muscle? *Exerc Sport Sci Rev* 3(123):127
30. Boushel R, Piantoadosi CA (2000) Near-infrared spectroscopy for monitoring muscle oxygenation. *Acta Physiol Scand* 168:615–622
31. Ferrari M, Mottola L, Quaresima V (2004) Principles, techniques, of near-infrared spectroscopy. *Can J Appl Physiol* 29:463–487
32. Yamamoto K, Niwayama M, Shiga T, Lin L, Kudo N, Takahashi M (1998) Accurate NIRS measurement of muscle oxygenation by correcting the influence of a subcutaneous fat layer. *Proc SPIE* 3194:166–173
33. Niwayama M, Lin L, Shao J, Kudo N, Yamamoto K (2000) Quantitative measurement of muscle hemoglobin oxygenation using near-infrared spectroscopy with correction for the influence of a subcutaneous fat layer. *Rev Sci Instrum* 71:4571–4575
34. Costes F, Barthelemy JC, Feasson L, Busso T, Geysant A, Denis C (1996) Comparison of muscle near-infrared spectroscopy and femoral blood gases during steady-state exercise in humans. *J Appl Physiol* 80:1345–1350
35. Theorell H (1938) Kristallinisches myoglobin. *Biochem Z* 268:73–82
36. Wilson JR, Mancini DM, McCully K, Feraro N, Lanoce V, Chance B (1989) Noninvasive detection of skeletal muscle underperfusion with near-infrared spectroscopy in patients with heart failure. *Circulation* 80:1668–1674
37. Harper AJ, Ferreira LF, Lutjemeier BJ, Townsend DK, Barstow TJ (2006) Human femoral artery and estimated muscle capillary blood flow kinetics following the onset of exercise. *Exp Physiol* 91:661–671
38. Kindig CA, Richardson TE, Poole DC (2002) Skeletal muscle capillary hemodynamics from rest to contractions: implications for oxygen transfer. *J Appl Physiol* 92:2513–2520

39. Bank W, Chance B (1994) An oxidative defect in metabolic myopathies: diagnosis by noninvasive tissue oximetry. *Ann Neurol* 36:830–837
40. Marcinek DJ, Amara CE, Matz K, Conley KE, Schenkman KA (2007) Wavelength shift analysis: a simple method to determine the contribution of hemoglobin and myoglobin to in vivo optical spectra. *Appl Spectrosc* 61:665–669
41. Binzoni T, Cooper CE, Wittkekind AL, Beneke R, Elwell CE, Van De Ville D, Leung TS (2010) A new method to measure local oxygen consumption in human skeletal muscle during dynamic exercise using near-infrared spectroscopy. *Physiol Meas* 31:1257–1269
42. Jue T, Anderson S (1990)  $^1\text{H}$  observation of tissue myoglobin: an indicator of intracellular oxygenation in vivo. *Magn Reson Med* 13:524–528
43. Dayhoff MO, Eck RV (1968) Atlas of protein sequence and structure. National Biomedical Research Foundation, Silver Spring
44. Kendrew JC (1963) Myoglobin and the structure of proteins. *Science* 139:1259–1266
45. Weissbluth M (1974) Cooperativity and electronic properties. *Mol Biol Biochem Biophys* 15:1–175
46. Horrocks JD (1973) Analysis of isotropic shifts. In: La Mar GN, Horrocks JD, Holm RH (eds) *NMR of paramagnetic molecules*. Academic, New York, pp 128–175
47. Jesson JP (1973) In: La Mar GN, Horrocks JD, Holm RH (eds) *The paramagnetic shift in NMR of paramagnetic molecules*. Academic, New York, pp 1–51
48. La Mar GN, Horrocks WD Jr, Holm RH (eds) (1973) *NMR of paramagnetic molecules*. Academic, New York
49. La Mar GN (1979) *Biological applications of magnetic resonance*. Academic, New York
50. Goff H, La Mar GN (1977) High-spin ferrous porphyrin complexes as models for deoxymyoglobin and deoxyhemoglobin: a proton nuclear magnetic resonance study. *J Am Chem Soc* 99:6599–6606
51. La Mar GN, Budd DL, Goff H (1977) Assignment of proximal histidine proton NMR peaks in myoglobin and hemoglobin. *Biochem Biophys Res Commun* 77:104–110
52. La Mar GN, Nagai K, Jue T, Budd DL, Gersonde K, Sick H, Kagimoto T, Hayashi A, Taketa F (1980) Assignment of proximal histidyl imidazole exchangeable proton NMR resonances to individual subunits in hemoglobins A, Boston, Iwate and Milwaukee. *Biochem Biophys Res Commun* 96:1172–1177
53. Ho C, Russu I (1981) Proton nuclear magnetic resonance investigation of hemoglobins. *Methods Enzymol* 76:275–312
54. Kreutzer U, Chung Y, Butler D, Jue T (1993)  $^1\text{H}$ -NMR characterization of the human myocardium myoglobin and erythrocyte hemoglobin signals. *Biochim Biophys Acta* 1161:33–37
55. Jue T, La Mar GN, Han K, Yamamoto Y (1984) NMR study of the exchange rates of allosterically responsive labile protons in the heme pockets of hemoglobin A. *Biophys J* 46:117–120
56. Patel DL, Kampa L, Shulman RG, Yamane T, Wyluda BJ (1970) Proton nuclear magnetic resonance studies of myoglobin in  $\text{H}_2\text{O}$ . *Proc Natl Acad Sci U S A* 67:1109–1115
57. Lindstrom TR, Ho C (1972) Functional nonequivalence of  $\alpha$  and  $\beta$  hemes in human adult hemoglobin. *Proc Natl Acad Sci U S A* 69(7):1707–1710
58. Kreutzer U, Wang DS, Jue T (1992) Observing the  $^1\text{H}$  NMR signal of the myoglobin Val-E11 in myocardium: an index of cellular oxygenation. *Proc Natl Acad Sci U S A* 89:4731–4733
59. Mole PA, Chung Y, Tran TK, Sailasuta N, Hurd R, Jue T (1999) Myoglobin desaturation with exercise intensity in human gastrocnemius muscle. *Am J Physiol* 277(1 Pt 2):R173–R180
60. Ponganis PJ, Kreutzer U, Sailasuta N, Knowler T, Hurd R, Jue T (2002) Detection of myoglobin desaturation in *Mirounga angustirostris* during apnea. *Am J Physiol Regul Integr Comp Physiol* 282:R267–R272
61. Ponganis PJ, Kreutzer U, Stockard TK, Lin PC, Sailasuta N, Tran TK, Hurd R, Jue T (2008) Blood flow and metabolic regulation in seal muscle during apnea. *J Exp Biol* 211(Pt 20):3323–3332
62. Masuda K, Takakura H, Furuichi Y, Iwase S, Jue T (2010) NIRS measurement of  $\text{O}_2$  dynamics in contracting blood and buffer perfused hindlimb muscle. *Adv Exp Med Biol* 662:323–328
63. Mancini DM, Wilson JR, Bolinger L, Li H, Kendrick K, Chance B, Leigh JS (1994) In vivo magnetic resonance spectroscopy measurement of deoxymyoglobin during exercise in patients with heart failure. *Circulation* 90:500–508
64. Ferrari M, Muthalib M, Quaresima V (2011) The use of near-infrared spectroscopy in understanding skeletal muscle physiology: recent developments. *Philos Trans R Soc Lond* 369:1–14
65. Nioka S, Wang DJ, Im J, Hamaoka T, Wang ZJ, Leigh JS, Chance B (2009) Simulation of Mb/Hb in NIRS and oxygen gradient in the human and canine skeletal muscle using H-NMR and NIRS. *Adv Exp Med Biol* 578:223–228
66. Hoofd L, Colier W, Oeseburg B (2009) A modeling investigation to the possible role of myoglobin in human muscle in near infrared spectroscopy (NIRS) measurements. *Adv Exp Med Biol* 530:637–643
67. Jue T (1994) Measuring tissue oxygenation with the  $^1\text{H}$  NMR signals of myoglobin. In: Gilles R (ed) *NMR in physiology and biomedicine*. Academic, New York, pp 199–207

68. Kreutzer U, Jue T (1991) <sup>1</sup>H-nuclear magnetic resonance deoxymyoglobin signal as indicator of intracellular oxygenation in myocardium. *Am J Physiol Cell Physiol* 261(6 pt 2):H2091–H2097
69. Chance B (1989) Metabolic heterogeneities in rapidly metabolizing tissue. *J Appl Cardiol* 4:207–221
70. Gayeski TEJ, Honig CR (1988) Intracellular Po<sub>2</sub> in long axis of individual fiber in working dog gracilis muscle. *Am J Physiol* 254:H1179–H1185
71. Flogel U, Merx MW, Godecke A, Decking UKM, Schrader J (2001) Myoglobin: a scavenger of bioactive NO. *Proc Natl Acad Sci U S A* 98(2):735–740
72. Garry DJ, Ordway GA, Lorenz JN, Radford NB, Chin ER, Grange RW, Bassel-Duby R, Williams RS (1998) Mice without myoglobin. *Nature* 395:905–908
73. Glabe A, Chung Y, Xu D, Jue T (1998) Carbon monoxide inhibition of regulatory pathways in myocardium. *Am J Physiol* 274:H2143–H2151
74. Tran TK, Sailasuta N, Kreutzer U, Hurd R, Chung Y, Mole P, Kuno S, Jue T (1999) Comparative analysis of NMR and NIRS measurements of intracellular pO<sub>2</sub> in human skeletal muscle. *Am J Physiol* 276:R1682–R1690